

# Method to assess the functional role of noisy brain signals by mining envelope dynamics

Andreas Meinel<sup>1</sup>, Henrich Kolkhorst<sup>1,2</sup> and Michael Tangermann<sup>1</sup>

<sup>1</sup>Brain State Decoding Lab, Department of Computer Science,

BrainLinks-BrainTools Cluster of Excellence, University of Freiburg, Germany

<sup>2</sup>Autonomous Intelligent Systems, Department of Computer Science, University of Freiburg, Germany

E-mail: {andreas.meinel|michael.tangermann}@blbt.uni-freiburg.de

April 2018

**Abstract.** *Objective.* Data-driven spatial filtering approaches are commonly used to assess rhythmic brain activity from multichannel recordings such as electroencephalography (EEG). As spatial filter estimation is prone to noise, non-stationarity effects and limited data, a high model variability induced by slight changes of, e.g., involved hyperparameters is generally encountered. These aspects challenge the assessment of functionally relevant features which are of special importance in closed-loop applications as, e.g., in the field of rehabilitation.

*Approach.* We propose a data-driven method to identify groups of reliable and functionally relevant oscillatory components computed by a spatial filtering approach. Therefore, we initially embrace the variability of decoding models in a large configuration space before condensing information by density-based clustering of components' functional signatures. Exemplified for a hand force task with rich within-trial structure, the approach was evaluated on EEG data of 18 healthy subjects.

*Main results.* We found that functional characteristics of single components are revealed by distinct temporal dynamics of their event-related power changes. Based on a within-subject analysis, our clustering revealed seven groups of homogeneous envelope dynamics on average. To support introspection by practitioners, we provide a set of metrics to characterize and validate single clusterings. We show that identified clusters contain components of strictly confined frequency ranges, dominated by the alpha and beta band.

*Significance.* Our method is applicable to any spatial filtering algorithm. Despite high model variability, it allows capturing and monitoring relevant oscillatory features. We foresee its application in closed-loop applications such as brain-computer interface based protocols in stroke rehabilitation.

**Keywords:** MEG/EEG, brain-computer interface, spatial filtering, oscillatory components, event-related (de)synchronization, machine learning

## 1. Introduction

Many cortical processes on microscopic and macroscopic levels can be described by oscillatory features [1, 2]. When recording rhythmic brain activity by non-invasive imaging techniques such as electroencephalography (EEG), such macroscopic signals enable to describe and characterize the underlying dynamics of cognitive or motor processes [3]. While many studies reported that oscillations are correlated with such processes [4], some studies have even proposed a causal relation [5].

A state-of-the-art approach to characterize oscillatory activity from EEG recordings is based on verifying the presence of time-locked, frequency-specific envelope modulations. They can be triggered by an internal or external event such as a simple visual cue. The induced power modulation effect is known as event-related (de)synchronization (ERD/ERS) [6, 7, 8]. Several approaches to observe and quantify ERD/ERS effects along the spatial, temporal and spectral domain have been proposed [9, 10, 11, 12] and thus enable to identify involved cortical regions evoking such power changes [13, 14]. Studies on ERD/ERS effects are mostly implemented with simple tasks. These typically result in a simple, cue-locked modulation of the band power [7] like an ERD upon movement onset. In contrast, more complex tasks with a richer temporal structure and a possibly richer resulting ERD/ERS structure have been studied far less frequently.

In the field of brain-computer interfaces (BCIs), oscillatory features are of specific interest when building a data-driven decoding pipeline using a spatial filtering algorithm [15]. This class of models generally learns a transformation to project multivariate EEG sensor data to an informative low-dimensional subspace [16, 17] while allowing for a neurophysiological model introspection [18]. Exploiting this low-dimensional representation as features for a decoding model enables to run a closed-loop system as currently deployed in the field of stroke rehabilitation [19].

Unfortunately, such spatial filtering algorithms have to deal with various issues including the low signal-to-noise ratio of high-dimensional M/EEG recordings, non-stationarities over time and generally small training data sets [20, 21]. As a result, even a slight change of the training data can cause a large variability of obtainable oscillatory features [22]. In addition, most approaches need to be configured by a set of algorithm-specific hyperparameters such as frequency bands, time intervals or regularization parameters, among others. Every hyperparameter set can result in different oscillatory features, such that applying a certain set may mean to miss relevant features. Conversely, modifying the hyperparameters actively bears the chance to detect other and even better features. Overall, the selection of the (few) best hyperparameter set(s) in a large space calls for an optimization criterion.

So far, most BCI applications were mostly tuned to solely maximize the *decoding accuracy*. This criterion has been a good choice, if the final goal of the BCI system is to gain rapid and precise control. Using performance as an optimization criterion, however, does not consider the functional role of oscillatory features directly [21]. While a manual

assessment of functional relevance is possible in small hyperparameter spaces, it turns to be impractical if they become large. Omitting any feature introspection, however, may be a missed opportunity, as details of their ERD/ERS characteristic might provide an equally beneficial criterion from a clinical perspective [23].

Stepping beyond decoding accuracy, current literature reveals a limited amount of studies that specifically explore reliable and physiologically plausible EEG features (both within and across sessions and subjects) within the huge space of possible features. Typically, this can be achieved by means of clustering approaches [21], e.g., to extract homogeneous groups of spatial filters [24, 25], to identify EEG features encoding a similar stimulus response [26], to partition oscillatory features into groups of similar spatial, temporal and spectral properties [12, 27, 14, 28, 29] or to identify artifactual components [30]. Consequently, it would be desirable to consider these two aspects, decoding performance and the functional role of features, in a unified approach.

In this paper, we contribute a novel data-driven approach to identify *reliable and functionally relevant* oscillatory features in the context of a complex visuo-motor hand force task. We hypothesize that the functional role of features can be assessed by the rich inner temporal envelope dynamics that is accompanied within a single trial along *multiple* events of a complex task.

In an offline analysis performed on individual subjects, we first explore a large configuration space to embrace the variability of oscillatory features derived by a spatial filter approach. Then their event-related envelope dynamics will be exploited by a clustering step to condense the large space to a small set of reliable oscillatory components that reveal homogeneous event-related envelope dynamics. Our approach finally allows for a component selection that takes the functional role of oscillatory features into account. Hence, we provide a tool to practitioners that might enhance the efficacy of closed-loop interaction protocols, e.g., in the context of BCIs for stroke rehabilitation.

## 2. Methods and materials

### 2.1. Visuo-motor hand force task

*Paradigm description* Subjects were seated at 80 cm distance from a 24 inch flat screen and performed a single session of a repetitive visuo-motor task named sequential visual isometric pinch task (SVIPT) [31]. They were asked to control a horizontally moving cursor by a force transducer which detects the applied force between thumb and index finger of the non-dominant hand. Throughout a session, brain activity was tracked via EEG for later offline analysis.

A SVIPT trial traverses three stages: the appearance of a light blue cursor initiates the *get-ready* phase with duration randomly varied between 2 and 3 s. As sketched in Fig. 1, an inactive cursor appears on the leftmost border of the target field T0 (referring to zero force) during this phase, and the force transduction into a horizontal cursor

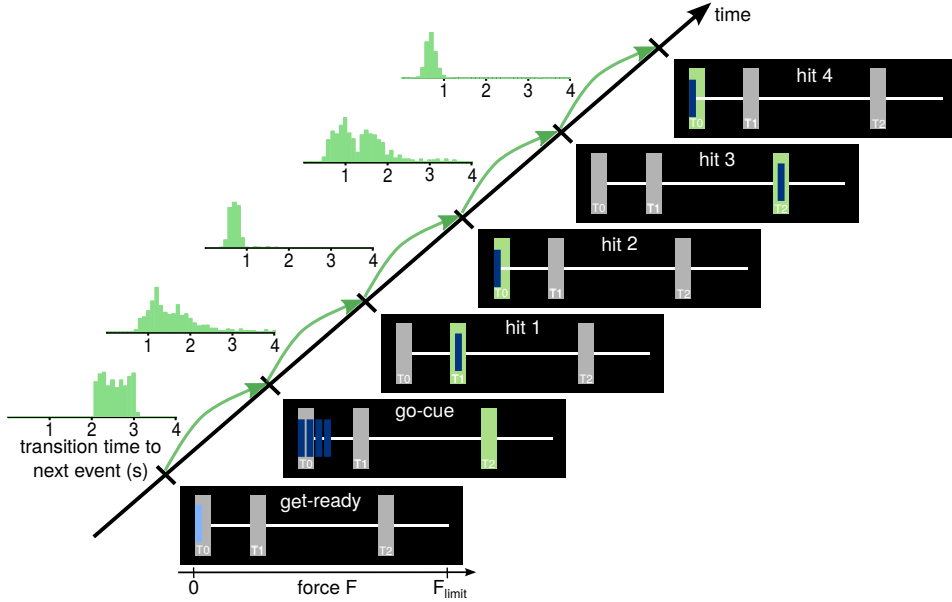


**Figure 1:** Time course of a single SVIPT trial (from bottom-left to top-right): The *get-ready* event encodes the beginning of a trial with an inactive cursor appearing on screen. The *go-cue* is encoded by a cursor color change and a subsequent translation of force to horizontal cursor positions. Subsequently, the subject has to maneuver the cursor through a sequence of four target fields. Once reaching a target field, a dwell time of 200 ms is required to evoke a *hit 1-4* event. To the right of every *within-trial* event, the user feedback on screen is shown. Histograms to the left of the time line indicate the distributions of transition times between two subsequent events. For clarity, the distances between single events on the time axis are not realistically spaced.

position is inactive. The subject was instructed to fixate the cursor and wait for a go cue which was indicated by switching the cursor's color to dark blue. Starting with the *go-cue* event, the horizontal cursor position can be controlled by applying force. Increasing force levels will move the cursor to the right end of the screen. Its rightmost position at  $F_{limit}$  is pre-calibrated at session start to 30 % of the user's maximal force.

The *go-cue* marks the running phase of the trial in which the subject is asked to maneuver the cursor through a sequence of target fields as fast and as accurate as possible. Thus, overshoots beyond target fields were to be avoided. A green shading visually indicates the current target field at any time during the *running* phase (see Fig. 1). Entering a target field with the cursor, a dwell time of 200 ms was required to evoke a successful hit event. The latter was indicated visually by a switch of the target field (another target fields appeared green shaded) or by the trial end. Each trial consisted of four hit events (*hit 1* to *hit 4*) and was randomly assigned to one of two target field sequences T1-T0-T2-T0 and T2-T0-T1-T0. Each trial ended with a *pause* phase upon fulfilling the complete target field sequence.

Overall, data of 18 subjects performing one session of SVIPT with 400 trials in total are utilized for the presented analysis. The study was approved by the Ethics

Committee of the University Medical Center Freiburg. Written informed consent was given by subjects prior to participation. For further details on the study, we refer to our initial paper [32].

*Data acquisition and preprocessing* Brain activity was acquired by multichannel EEG amplifiers (BrainAmp DC, Brain Products) with a sampling rate of 1 kHz from 63 passive Ag/AgCl electrodes (EasyCap) placed according to the extended 10-20 system. Offline preprocessing comprised high-pass filtering the raw EEG signals at 1 Hz before low-pass filtering them at 100 Hz and sub-sampling them to 500 Hz sample frequency. For frequency filtering, linear butterworth filters of 5th order were applied. Noisy channels were removed by a variance criterion. Furthermore, artifact cleaning was done by an independent component analysis (ICA) decomposition on data of the first run of each session. The ICs were rated for artifactual origin with the automated artifact detection framework MARA [33, 34]. Based on MARA ratings, a maximum number of 10 probably artifactual ICs were removed from the data before projecting it back into the original sensor space. Only this pre-cleaned data was used in the next steps. For extracting the event-wise envelope information, a supervised spatial filter algorithm was trained. It received data of each channel after segmentation to the interval of  $[-1000, 500]$  ms relative to the *go-cue* event for each trial. For each of these resulting epochs, a variance and a min-max criterion was applied to remove outliers. Finally, we extracted the reaction time (RT) from the SVIPT trial corresponding to each epoch. For further details see [32].

## 2.2. Optimized spatial filtering for single-trial EEG analysis

Let  $\mathbf{x}(t) \in \mathbb{R}^{N_c}$  describe multivariate EEG data acquired from  $N_c$  sensors at time  $t$ . In addition, let  $\mathbf{x}(t)$  be filtered to a narrow frequency band  $[f_0 - \Delta f, f_0 + \Delta f]$  characterized by a central frequency  $f_0$  and a bandwidth  $\Delta f$ . Following the generative model of the EEG [35], a spatial filter  $\mathbf{w} \in \mathbb{R}^{N_c}$  represents a linear projection of the sensor space data  $\mathbf{x}(t)$  to a one-dimensional source component  $\hat{s}(t) = \mathbf{w}^\top \mathbf{x}(t)$ . Moreover, we assume the data to be segmented into  $N_e$  single epochs such that  $\mathbf{X}(e) \in \mathbb{R}^{N_c \times T_e}$  denotes an epoch-wise matrix with  $T_e$  sample points.

Spatial filtering is a widely established class of algorithms for single-trial EEG analysis [15], aiming at the enhancement of the intrinsically low signal-to-noise ratio of multi-channel brain activity recordings. Varying in the formulation of their underlying optimization criteria, typical algorithmic solutions for unsupervised scenarios include principal component analysis (PCA), ICA or canonical correlation analysis (CCA) [16, 36]. In the context of BCI, supervised algorithms such as common spatial patterns (CSP) [37] or source power comodulation (SPoC) [38] are state-of-the art approaches. Regardless of the algorithm choice, all methods have in common that a set of hyperparameters needs to be determined, which influences the spatial filter optimization. Prominent examples are to choose a suitable subject-specific frequency band of interest or to select a particular rank if the method delivers a full rank decomposition of the

input space. Please note, that choosing different sets from the large search space of possible hyperparameter configurations can lead to very different resulting components.

In the following, we present a method to identify consistent spatial filters within a pre-defined hyperparameter space. Even though this approach can be *utilized for any spatial filtering method*, we exemplarily show and evaluate its application for a regularized version of SPoC named NTik-SPoC [39, 40]. This supervised spatial filtering algorithm allows to regress upon a trial-wise target variable given multi-variate brain signal data. As an application scenario, we chose to decode trial-wise motor performance represented by reaction time from multi-channel EEG recordings segmented to a time interval close to the SVIPT *go-cue*. A more detailed description can be found in our initial paper [32].

*Hyperparameter space for oscillatory component analysis* For the computation of a single spatial filter  $\mathbf{w}$ , a set of different hyperparameters is involved (see Figure 2). In this paper, we considered the following hyperparameters for the aforementioned SVIPT decoding scenario to explore large variance in the trained decoding models:

- (i) In the temporal domain, initial data segmentation into  $N_e$  epochs requires to specify a time interval  $[t_0, t_0 + \Delta t]$  with starting time point  $t_0$  and interval length  $\Delta t$ . For motor performance decoding in SVIPT, the recorded EEG data were segmented relative to the *go-cue* event with fixed  $\Delta t = 1$  s. Time point  $t_0$  was chosen among the values  $\{-1, -0.75, -0.5\}$  s.
- (ii) The frequency domain is characterized by the central frequency  $f_0$  and bandwidth  $\Delta f$ . Overall, logarithmically increasing and overlapping frequency bands ranging from  $\approx 1$ –100 Hz were evaluated.
- (iii) The chosen spatial filtering method generally provides a full-rank decomposition, thus the rank  $k$  can be seen as another hyperparameter for thresholding the composition. We considered spatial filters of the first  $k = 1, \dots, 8$  ranks for further analysis.
- (iv) NTik-SPoC requires the tuning of the regularization strength  $\alpha$ . Based on findings reported in [40, 39], choosing the regularization strength  $\alpha \in [10^{-8}, 10^{-3}]$  allows to outperform non-regularized SPoC wrt. decoding accuracy.
- (v) Upon each hyperparameter configuration, a 5-fold chronological cross-validation procedure was employed for the calculation of a spatial filter. As typically spatial filter optimization can be formulated as a generalized eigenvalue problem, a set of spatial filters  $\{\mathbf{w}_{k,q}\}$  can be derived from each fold  $q$ , with  $k$  corresponding to the rank in the decomposition.

In summary, the different hyperparameter configurations span the configuration space  $\Omega = \{(t_0, f_0, \Delta f, k, \alpha, q)\}$  with an overall number of  $|\Omega| = 81,000$  configurations. We will refer to a single configuration by  $\omega_j \in \Omega$ ,  $(j = 1, \dots, |\Omega|)$ . It determines a single spatial filter calculation. Hereafter, every spatial filter  $\mathbf{w}$  intrinsically corresponds to a single configuration  $\omega_j$ .

*Regularized source power comodulation (NTik-SPoC)* NTik-SPoC is a regularized SPoC variant which was introduced and benchmarked in [39]. The supervised spatial filter approach allows to regress upon an epoch-wise univariate behavioral variable  $z(e)$ . For our SVIPT data scenario, we will consider reaction time (RT) here.

NTik-SPoC optimizes a spatial filter  $\mathbf{w}$  based on epoched data  $\mathbf{X}(e)$  such that the epoch-wise source power  $\phi_j(e) = \text{Var}(\mathbf{w}^\top \mathbf{X}(e))$  maximally co-modulates with the target variable  $z(e)$ . This is achieved by solving  $\mathbf{w}^* = \underset{\mathbf{w} \in \mathbb{R}^{N_c}}{\text{argmax}} \text{Cov}(\phi_j, z)$  under the norm constraint  $\mathbf{w}^\top \tilde{\Sigma}_{avg} \mathbf{w} \stackrel{!}{=} 1$  with a shrunk covariance matrix  $\tilde{\Sigma}_{avg}$ :

$$\tilde{\Sigma}_{avg} = (1 - \alpha)\Sigma_{avg} + \alpha I \quad (1)$$

This shrinkage operation regularizes the average covariance matrix  $\Sigma_{avg} := \langle \Sigma(e) \rangle$  — averaged across all  $N_e$  epochs — towards the identity matrix  $I \in \mathbb{R}^{N_c \times N_c}$ . The shrinkage intensity is modulated by the regularization parameter  $\alpha$ . Here,  $\Sigma(e) = (N_s - 1)^{-1} \mathbf{X}^\top(e) \mathbf{X}(e)$  denotes an epoch-wise covariance matrix. The above optimization problem can be formulated as a generalized eigenvalue problem (GEP) such that solving for  $\mathbf{w}$  delivers a full set  $\{\mathbf{w}_k^*\}_{k=1, \dots, N_c}$  of  $N_c$  spatial filters. In this case, the rank  $k$  is assigned in descending order of the resulting eigenvalues when solving the GEP. NTik-SPoC includes a Tikhonov regularization as described by Eq. 1 combined with an additional trace normalization of  $\Sigma(e)$  and of the average covariance matrix  $\Sigma_{avg}$ .

As NTik-SPoC is a linear method, each spatial filter can be visually interpreted by a corresponding average activity pattern [18]:

$$\mathbf{a} = \Sigma_{avg} \mathbf{w} \quad (2)$$

Once a filter  $\mathbf{w}_{tr}$  has been computed on training data  $\mathbf{X}_{tr}(e)$ , it allows to estimate the target variable  $z(e)$  on novel, unseen test data  $\mathbf{X}_{te}(e)$  by simply estimating the epoch-wise source power  $\phi_j(e)$ :

$$z_{est}(e) = \phi_j(e) \approx \text{Var}(\mathbf{w}_{tr}^\top \mathbf{X}_{te}(e)) = \mathbf{w}_{tr}^\top \Sigma_{te}(e) \mathbf{w}_{tr} \quad (3)$$

*Evaluation scheme for spatial filter computation* NTik-SPoC was evaluated within a 5-fold chronological cross-validation procedure such that the data is split in train  $\{\mathbf{X}_{tr}, z_{tr}\}$  and test sets  $\{\mathbf{X}_{te}, z_{te}\}$ . After estimating the labels  $z_{est}$  on different test data points  $\mathbf{x}_{te}$  according to Eq. 3, the decoding performance of a single filter  $\mathbf{w}_{tr}$  can be assessed by the z-AUC metric [32, 39]. This measure characterizes the separability of the estimated labels when comparing them to the known test labels  $z_{te}$ . In analogy to the area under the ROC curve (AUC) [41], a perfect decoding is reflected by a value of 1, while chance level is reflected by 0.5. Hereafter, we will omit the train/test subscripts to simplify the notation.

### 2.3. Method for mining oscillatory components

Our method to identify groups of functionally relevant oscillatory components is depicted in Fig. 2. It consists of three steps: First, oscillatory components from EEG data of

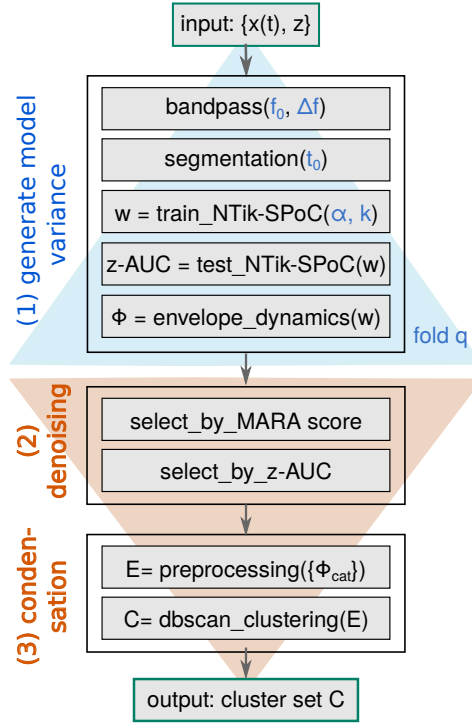


**Figure 2:** Schematic procedure with pseudo-code to assess groups of functionally relevant oscillatory components. The subject-specific data  $x(t)$  and labels  $z$  enter part (1) to generate oscillatory components in a large hyperparameter space. This step generates variance along the computed spatial filters. In blue, all included hyperparameters for computing a single spatial filter  $w$  are depicted. Part (2) is a denoising step by reducing the overall configuration space. The final step (3) condenses information by feature preprocessing and a clustering step to obtain clusters  $c_k$ .

a single subject are computed across a large hyperparameter space. This results in a broad variety of spatial filter examples and embraces the variability of the decoding method. Details on the screened configuration space are given in Sec. 2.2. Second, the large component space is denoised by restricting the analysis to *reliable* components via selection criteria on single components. Third, for all remaining components the event-related envelope dynamics of each source component is exploited for a clustering step. Therefore, envelope features are preprocessed and condensed. The goal is to finally identify clusters of oscillatory components which reveal distinct and stable envelope dynamics. In the following, the details on step (2) and (3) as sketched in Fig. 2 are explained in detail.

*Denoising clustering input data* The overall spanned hyperparameter space  $\Omega$  elicits a large variation of derived spatial filters  $\mathbf{w}$  of which a large fraction might be non-stable or of artifactual origin. To control for their reliability, the overall component space was reduced by deploying two hard selection criteria for the SVIPT decoding scenario: First, each spatial filter is expected to exceed a robust decoding performance



level above chance. Therefore, each spatial filter is required to result in a decoding performance above a threshold level of  $\text{z-AUC}_{\text{threshold}} = 0.6$  on test data. The threshold was determined on a group-level analysis [32]. Second, the neural origin of a spatial filter is verified once more by applying MARA [34]. This tool enables to derive a posterior artifact probability  $p_{\text{post}}$  for a given single oscillatory component. To restrict the resulting component space to mostly neural components with a high certainty, we required a probability of  $p_{\text{post}} \leq 10^{-5}$  for each component.

In summary, the two selection steps reduced the original configuration space  $\Omega$  to a subject-specific subset  $\Omega_{\text{sel}} \subset \Omega$  which comprises all hyperparameter configurations that survived the component selection. Hereafter, the configuration index  $j$  refers to the set  $\Omega_{\text{red}}$ .

*Extracting envelope dynamics* The temporal dynamics of an oscillatory source component  $\mathbf{w}$  derived by configuration  $\omega_j \in \Omega_{\text{sel}}$ , given sensor data  $\mathbf{x}(t)$ , can be derived via  $\hat{s}(t) = \mathbf{w}^\top \mathbf{x}(t)$ . It requires to bandpass filter the data  $\mathbf{x}(t)$  to the same frequency band  $[f_0 - \Delta f, f_0 + \Delta f]$  on which the spatial filter  $\mathbf{w}$  has been trained initially. As an alternative to the variance approximation, the power time course of  $\hat{s}(t)$  can be estimated by computing the magnitude of its Hilbert transformation  $\mathcal{H}(\cdot)$ :

$$\phi_j(t) = \mathcal{H}(\hat{s}(t)) = \mathcal{H}(\mathbf{w}^\top \mathbf{x}(t)) \quad (4)$$

For the described SVIPT data, each spatial filter  $\mathbf{w}$  was trained on data segments extracted from the vicinity of the *go-cue* event. However, as depicted in Fig. 1, a single SVIPT trial also contains a rich inner structure of multiple events  $m$  (*get-ready*, *go-cue* and *hit1* to *hit4*). We expect that this within-trial structure is at least partly captured by the temporal envelope dynamics of single oscillatory components. In other words, we test for the generalization strength of  $\mathbf{w}$  on unseen data. Therefore, the envelope time course  $\phi_j(t, m)$  was segmented in a time interval  $t \in [-300, 2000]$  ms relative to each event  $m$  and averaged across the  $N_e = 400$  epochs. This resulted in  $\phi_j(t, m)$  as exemplarily sketched for one component in Fig. 3(A).

*Features for clustering* For each configuration  $\omega_j \in \Omega_{\text{sel}}$  the corresponding event-related envelope dynamics  $\phi_j(t)$  were extracted as depicted in Fig. 3(A). As clustering methods generally depend on the evaluation of a distance metric which is unreliable for high-dimensional feature spaces, a widely established strategy is then to restrict the dimensionality of the input feature space [42]. Therefore, two steps were taken:

- (i) The logarithmic epoched band power time series of the four most relevant events  $M = \{\text{'get-ready'}, \text{'go-cue'}, \text{'hit3'}, \text{'hit4'}\}$  were temporally subsampled to 18 time samples per event. This step is schematically shown in Fig. 3(A) and resulted in a concatenated feature vector  $\phi_{\text{cat},j} = \phi_{\text{cat}}(\omega_j) \in \mathbb{R}^{D_{\text{cat}}}$  with  $D_{\text{cat}} = 76$ . After computing mean  $\mu$  and standard deviation  $\sigma$  of this long feature vector  $\phi_{\text{cat},j}$ , it was standardized to zero mean and unit variance. Overall, applying this procedure

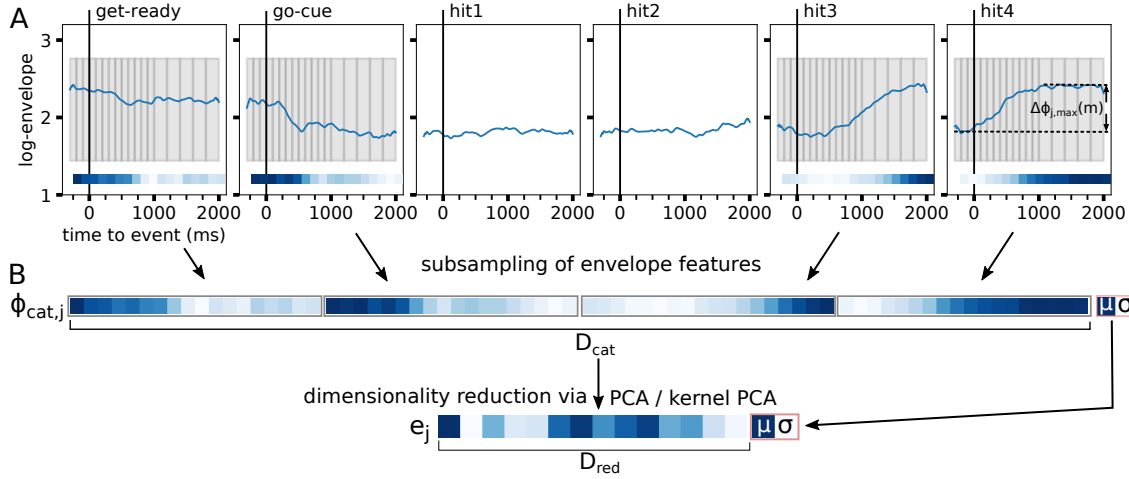


**Figure 3:** Schematic feature extraction and compression from envelope dynamics of a single oscillatory component. (A) The session average log-power of an oscillatory component was epoched and aligned to the various within-trial SVIPT events. In grey, time intervals for temporal subsampling of the event-related time series are depicted. Each subsample will serve as a feature in the following. (B) Schematic procedure for the feature preprocessing of a single oscillatory component. After the beforementioned temporal subsampling into 18 time intervals per event, the resulting features of the four most relevant events are concatenated to  $\phi_{cat,j}$ . This feature vector was standardized to zero mean and unit variance as illustrated by the color coding. To preserve this information, the original mean and standard deviation across all features are added as two extra features. After a dimensionality reduction step,  $D_{red} = 10$  condensed features plus the two standardization features build the final feature vector  $e_j$  which serves as an input sample for the clustering.

to all selected configurations  $\omega_j \in \Omega_{sel}$ , this yielded a subject-specific data set  $\Phi = \{\phi_{cat,j}\}$  with  $j = 1, \dots, |\Omega_{sub}|$ .

- (ii) A dimensionality reduction step on the concatenated feature vector  $\Phi$  was performed by either PCA or by kernel PCA to  $D_{red} = 10$  components. Kernel PCA was computed by choosing a radial basis function kernel with  $\gamma = 1/D_{red}$ . The final feature vector  $e_j$  was composed of the  $D_{red}$  subspace features based on  $\Phi$  and two additional features of the standardization step ( $\mu$  and  $\sigma$ ). This resulted in  $e_j \in \mathbb{R}^D$  with  $D = 12$  dimensions. We end up with a subject-specific data set  $E = \{e_j\}$  of  $|\Omega_{sel}|$  samples.

*Density-based clustering* In order to find sets of components with homogeneous envelope dynamics, we aim to group them by searching non-overlapping clusters of components. Assuming that a rich within-trial envelope structure is only expected for a small fraction of all configurations, it may not be necessary to assign each configuration  $\omega_j$  to a cluster. Let a clustering of  $E$  return a set of disjoint clusters that splits  $E$  into  $|C|$  groups with  $C = \{c_k\}$  and  $k = 1, \dots, |C|$ . Furthermore,  $d_{euc}(e_i, e_j)$  denotes the euclidean distance in the reduced feature space between samples  $e_i$  and  $e_j$ .

For partitioning the data set  $E$ , the DBSCAN [43, 44] algorithm was utilized, which realizes a density-based clustering [45]. The algorithm groups dense regions of data to clusters by checking for every sample of a data set if: (1) within an  $\epsilon$  distance of this sample a minimum number of other samples  $m_{pts}$  is contained or (2) at least one neighboring sample is enclosed. If the first case matches, the sample is called a *core sample* while for the second case it is referred to as a *border point*. If none of the two criteria are fulfilled, the sample receives an *outlier* label. As such, the density-based definition of a cluster requires that all samples within a cluster are within a distance smaller than  $\epsilon$ . DBSCAN does not make any assumption on the cluster shape, thus it can identify non-linearly separable clusters. In this paper, DBSCAN was evaluated on Euclidean distances between samples in a condensed envelope feature space.

DBSCAN involves two hyperparameters,  $m_{pts}$  and  $\epsilon$ . Regarding  $m_{pts}$ , we followed the suggestion of Sander et al. to take the feature dimensionality  $D$  into account by setting  $m_{pts} := 2D$  [46].

The choice of  $\epsilon$  is the more sensitive parameter, as the number of clusters  $|C|$  diminishes strongly for an increased  $\epsilon$  [44]. Overall, we expect that the envelope dynamics will not reveal a rich structure for all hyperparameter configurations  $\omega_j \in \Omega_{sel}$ , e.g., if ERD/ERS effects are not present. Hence, we expect to have a rather large outlier cluster. Thus, a simple maximization of the average silhouette scores  $S$  (definition see below) — which has been used successfully for many other applications of DBSCAN — will most probably be dominated by the outlier class. Instead, we aim to find the maximal number of homogeneous clusters  $N_{hom}$  which translates to the following optimization criterion for  $\epsilon$ :

$$N_{hom}(\epsilon) = \sum_{c_k \in C(\epsilon)} \Theta(\min_{e_i \in c_k} (S(e_i, c_k)) \geq S_{hom}) \rightsquigarrow \epsilon^* = \arg \max_{\epsilon \in [\epsilon_{min}, \epsilon_{max}]} N_{hom}(\epsilon)$$

with the unit-step function  $\Theta(x) = 1$  for  $x \geq 0$  and  $\Theta(x) = 0$  for  $x < 0$ .  $N_{hom}$  refers to the total number of clusters, where the sample  $e_i$  with smallest silhouette  $S(e_i, c_k)$  of each cluster  $c_k$  is required to exceed a threshold silhouette score  $S_{hom}$ . For this paper, a subject-independent threshold of  $S_{hom} = 0.2$  was set in order to allow for comparable clustering results such as  $|C|$  per subject. This threshold value enforces a slightly smaller within-cluster distance compared to the nearest neighbor distance. The interval  $[\epsilon_{min}, \epsilon_{max}]$  was automatically determined by an ordered  $k$ -distance plot which is based on the  $k$ -th nearest neighbor distance (NND) for each sample in  $E$ . This procedure was described by [43, 46, 44] together with setting  $k = D$ . For  $\epsilon_{max}$ , we detected the first substantial increase of the  $k$ -distance plot (starting with smallest distances) by a variance criterion in order to find the end of the “valley” of lowest distances. As lower boundary,  $\epsilon_{min}$  was determined by the 2nd percentile of the  $D$ -th NND distribution. Finally,  $\epsilon$  was evaluated at 60 values from the subject-specific interval  $[\epsilon_{min}, \epsilon_{max}]$ .

*Validation metrics for clustering* Given the condensed log-envelope data set of different oscillatory components, the ground truth cluster labels are unknown. Thus we require

a label-free validation metrics [47, 48] to judge the quality of the clustering outcome. In this paper, three different categories of validation metrics are considered [49]: (1) internal validation metrics based on features used for the clustering, (2) external validation metrics which utilize features that have not been used for the partitioning step and (3) context-specific metrics which are defined by domain-knowledge given specific characteristics of the oscillatory component data sets. In the following, for each metric a reference symbol is given in brackets as well as an arrow that indicates the direction towards a more preferable clustering (e.g.,  $\uparrow$  denotes “higher is better”):

- Silhouette score  $S(c_k) \uparrow$  [50]: Given an arbitrary sample  $e_i$  assigned to cluster  $c_k$ , this internal clustering validation score relates the within-cluster similarity  $a(e_i, c_k) = |c_k|^{-1} \sum_{e_j \in c_k \setminus \{e_i\}} d_{euc}(e_i, e_j)$  to the nearest neighbor dissimilarity  $b(e_i, c_k)$ :

$$b(e_i, c_k) = \min_{c_l \in C \setminus c_k} [|c_l|^{-1} \sum_{e_j \in c_l} d_{euc}(e_i, e_j)]$$

The silhouette score  $S(e_i, c_k)$  for a sample  $e_i$  belonging to cluster  $c_k$  is defined as:

$$S(e_i, c_k) = \frac{b(e_i, c_k) - a(e_i, c_k)}{\max[a(e_i, c_k), b(e_i, c_k)]} \quad (5)$$

It can be verified easily that  $-1 \leq S(e_i, c_k) \leq +1$ , where a “perfect” clustering will return a value of +1. Among other metrics, the silhouette metric has been shown to serve as a reliable *internal* clustering validation method—computed upon features used for the clustering—for various classes of clustering algorithms [51, 49]. Furthermore, the within-cluster silhouette score  $S(c_k) = |c_k|^{-1} \sum_{e_i \in c_k} S(e_i, c_k)$  can be determined with low computational effort.

- Intra-cluster mean squared error IC-MSE  $\downarrow$ : For the envelope clustering, a number of preprocessing steps were applied in order to reduce the dimensionality of the original time resolved event-related envelopes (see Fig. 3). To verify the intra-cluster homogeneity of cluster  $c_k$  upon the original event-wise log-power time series, the event-specific mean  $\phi_{avg}(c_k, t, m) = |c_k|^{-1} \sum_{\omega_j \in c_k} \phi_j(t, m)$  for cluster  $c_k$  is utilized to compute the mean squared error across the full set of events M and time samples T:

$$\text{IC-MSE}(c_k) = (|c_k| |M| |T|)^{-1} \sum_{\omega_j \in c_k} \sum_{m \in M} \sum_{t \in T} (\phi_j(t, m) - \phi_{avg}(c_k, t, m))^2 \quad (6)$$

To summarize, IC-MSE corresponds to the intra-cluster envelope variance. It can be seen as an external validation metric as it is based on envelope features which were not utilized for the clustering.

- Intra-cluster pattern heterogeneity ICPH: As a context-specific validation metric, for each sample  $e_j$  of a cluster  $c_k$ , the spatial activity pattern  $\mathbf{a}_j$  can be computed via Eq. 2. As a measure of the within-cluster heterogeneity of spatial activity patterns for a cluster  $c_k$ , the cosine angle  $\theta$  as defined in [39] between each  $\mathbf{a}_j$  to a cluster

representative pattern  $\mathbf{a}^*(c_k)$  is averaged as follows:

$$\text{ICPH}(c_k) = |c_k|^{-1} \sum_{e_j \in c_k} \theta(\mathbf{a}_j, \mathbf{a}^*(c_k)) \quad (7)$$

The representative pattern  $\mathbf{a}^*$  is defined by identifying the sample  $e^* \in c_k$  with minimal Euclidean distance wrt. clustering features to all other samples of the same cluster.

- Intra-cluster central frequency variation  $\text{std}(f_0(c_k)) \downarrow$ : Another context-specific validation will be accessible via the central frequency hyperparameter  $f_0$  which is involved in the spatial filter optimization. When capturing the within-cluster variation of  $f_0$  by  $\text{std}(f_0(c_k))$ , this value is expected to be rather low as EEG features are confined with respect to their spectral occurrence.
- Event-specific maximal envelope difference  $\Delta\phi_{\max}(m, c_k)$ : This metric serves to functionally characterize single clusters by their underlying ERD/ERS dynamics. As exemplarily sketched for *hit 4* in Fig. 3, the maximum envelope difference  $\Delta\phi_{j,\max}(m)$  for each event  $m$  and configuration  $\omega_j \in c_k$  of a cluster  $c_k$  can be assessed. Averaging across all cluster configurations reveals the event-specific maximal within-cluster logarithmic power differences  $\Delta\phi_{\max,\text{avg}}$ :

$$\Delta\phi_{\max,\text{avg}}(m, c_k) = |c_k|^{-1} \sum_{\omega_j \in c_k} \Delta\phi_{j,\max}(m) \quad (8)$$

Given a homogeneous cluster,  $\Delta\phi_{\max,\text{avg}}(m) < 0$  refers to an ERD effect for event  $m$ , while  $\Delta\phi_{\max,\text{avg}}(m) > 0$  describes an ERS effect.

*Evaluation scheme for clustering step* In this paper, we evaluated our proposed methodology on data of 18 subjects. For each subject, the size of the selected configuration space  $|\Omega_{\text{sel}}|$  was substantially different (see results in Sec. 3.1.4). In order to compare clustering runs across subjects, we randomly sampled  $N = 2000$  feature vectors  $e_j$  while keeping their order before entering the clustering. This procedure was repeated twelve times per subject.

### 3. Results

The results are organized in two parts: First, we present the most relevant findings for practitioners (e.g. in the field of BCIs for rehabilitation). Here, representative subject-specific clusters of oscillatory components are described, and we present a way to *functionally* characterize the grouped event-related envelope dynamics. Thereby, we demonstrate the applicability of our method. Second, we validate and characterize our approach by presenting a group level analysis across clusterings of all 18 subjects.

#### 3.1. Findings for the practitioner

For the practitioner, it may be of particular interest to gain understanding, which insights our method can provide on the level of single subjects and on the group level.

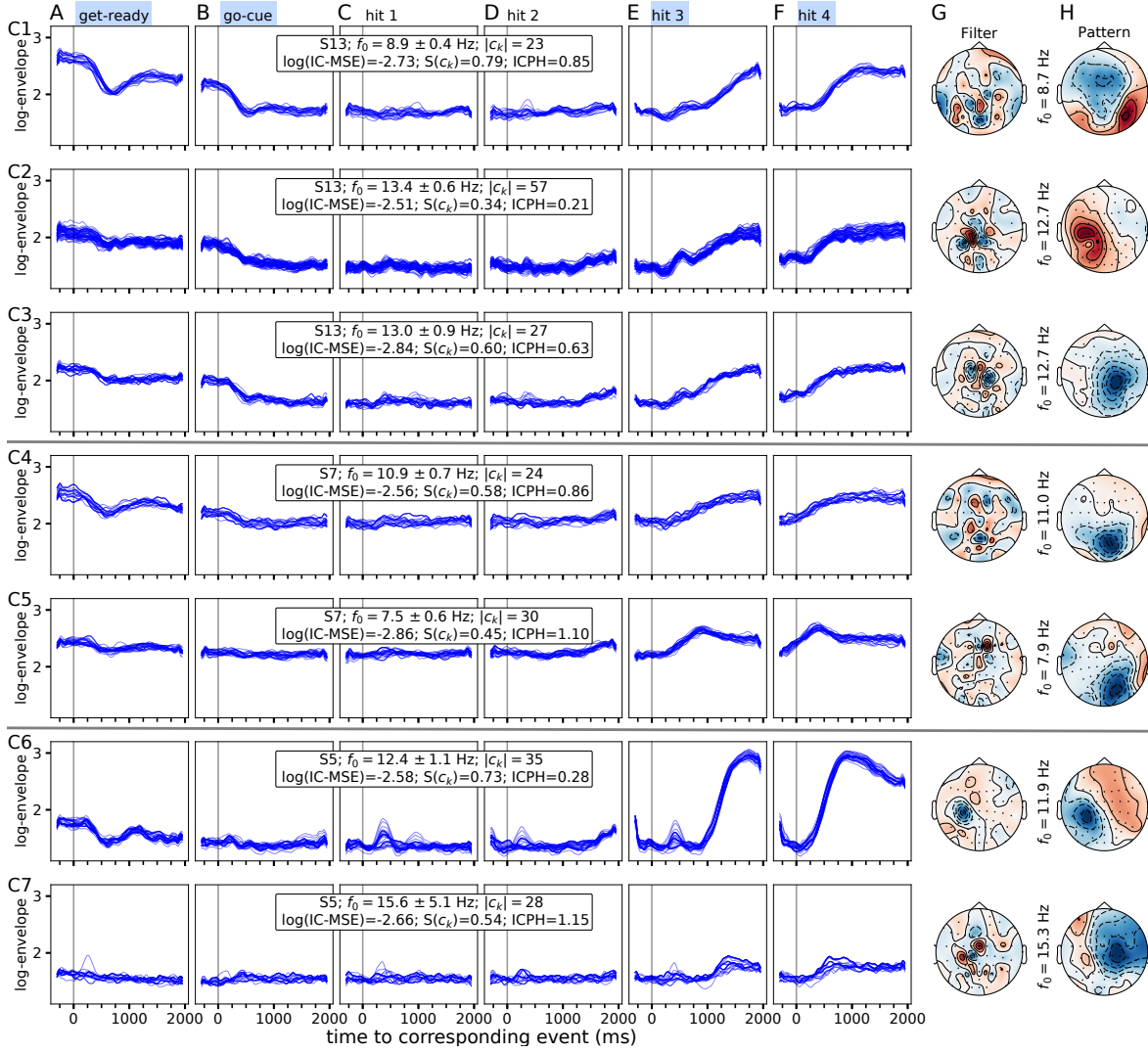


**Figure 4:** Representative event-related envelope dynamics of all hyperparameter configurations for single subject-specific clusters  $c_k$  reported in rows (C1)–(C7). Columns (A)–(F) report the cluster-wise envelope dynamics for within-trial SVIPT events, while in (G) the spatial filter and in (H) the related activity pattern of cluster representatives are shown. In addition, the central frequency  $f_0$  of the cluster representative is annotated. In all subplots of columns (A)–(F), every blue line refers to the log-envelope dynamics  $\phi_j(t, m)$  of one single hyperparameter configuration  $\omega_j \in c_k$ . Only events shaded in blue were included for the clustering step. The text box on top of each row provides the subject code, the mean and standard deviation of the central frequency  $f_0$  across all cluster samples, the cluster size as well as three validation metrics.

**3.1.1. Envelope dynamics of clusters** After applying the described within-subject approach, we report the original (non-condensed) within-trial event-related envelope dynamics of subject-specific clusters in Fig. 4.

For all examples, the spatial filter and corresponding activity pattern of the cluster representatives — obtained by selecting the sample with minimal Euclidean distance

in the feature space — are shown in columns (G) and (H). Rows (C1)–(C7) present different instances of exemplary clusters. They were chosen to represent a broad range of typically observed effects in terms of band power amplitudes, underlying frequency ranges and cluster homogeneity. Specifically, rows (C1)–(C3) refer to clusters of subject S13, while (C4)–(C5) are gained from subject S7 and (C6)–(C7) correspond to S5.

Considering the transition times between single events as provided by Fig. 1, the time between *hit 1* and *hit 2* as well as between *hit 3* and *hit 4* is on average around 800 ms. Thus, the event-locked envelopes in (C) and (D), respectively (E) and (F), contain overlapping information.

Based on Fig. 4, the following observations can be reported:

First, regarding all shown exemplary clusters, the envelope dynamics aligned to the different within-trial SVIPT events reveal distinct and time-locked ERD or ERS effects which can be separated well by the clustering approach. For the cases reported in Fig. 4, ERD effects dominate for *get-ready* and *go-cue* events, while *hit3* and *hit4* elicit ERS effects.

Second, the displayed examples demonstrate that the event-related envelope dynamics reveal substantially different shapes both within and across subjects. Taking a closer look at the selected cluster instances of S13 with clusters (C1)–(C3) at the *get-ready* event, there are different effects visible. While components grouped into (C2) and (C3) reveal a slight step-like behaviour, cluster (C1) comes with a strong ERD followed by an ERS effect. Regarding *hit 4* of (C6) and (C7), the examples for subject S5 nicely illustrate that amplitude differences can be substantially different across clusters/configurations. While clusters (C4) and (C5) of subject S7 are characterized by an ERS effect time-locked to *hit 3*, all remaining examples reveal the ERS at *hit 4*.

Third, we can report under which conditions our clustering approach works best, e.g., when comparing the cases (C1) and (C2). They nicely demonstrate that smaller cluster sizes correspond to more homogeneous clusters as visually observable and documented by, e.g., the IC-MSE values.

Fourth, similar silhouette and IC-MSE scores do not directly imply a high pattern homogeneity (low ICPH values), as can be seen comparing clusters (C1) and (C6).

*3.1.2. Functional assessment of clusters* Cluster-specific ERD/ERS intensities indicate the functional role of the contained components and thus provide a way to characterize single clusters post-hoc. An example is given in Fig. 5(A). It exemplarily describes the logarithmic power differences within *get-ready* and *hit4* events.

The distributions on the x- and y-axis reveal ERD effects time-locked to *get-ready* and *go-cue* (not shown here) and a subsequent ERS effect with the last hit event per trial. Captured by the tails of the distributions reported in Fig. 5(A), a small fraction of clusters behaves differently and reveals an ERS for *get-ready*, which might be caused by remaining artifactual components.

As already stated for the examples given in Fig. 4, the event- and cluster-specific maximal power differences  $\Delta\phi_{max,avg}(m, c_k)$  vary from subject-to-subject and even

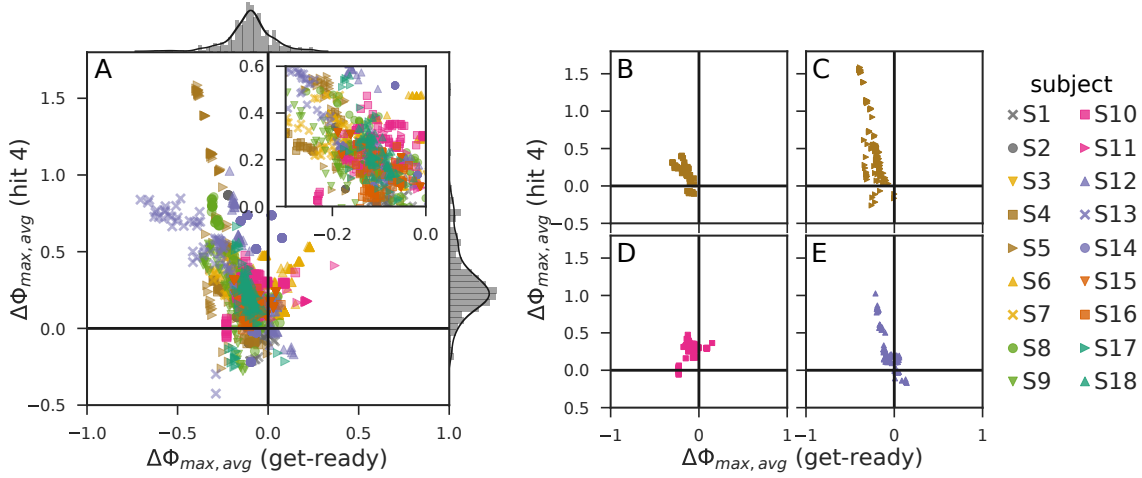


**Figure 5:** Scatter plots revealing cluster-specific ERD/ERS effects exemplarily for two specific SVIPT events. (A) The plot is built on pooled data from all clusterings across subjects. A single data point refers to an individual cluster and is encoded by its underlying subject. The inset plot shows a magnified version of the central area. Attached to both axes, the corresponding distributions across all displayed configurations are shown. Plots (B)–(E) show exemplary scatter plots for single subjects.

within the same subject as exemplarily reported in Fig. 5(B)–(E). The markers related to a single subject in Fig. 5 are really close or even overlapping for some cases, which is expected due to finding identical clusters over the twelve clustering runs per subject.

*3.1.3. What kind of components are assigned to clusters?* From a domain expert’s point of view, it is interesting to know, which components are assigned to clusters by the DBSCAN method. This information becomes accessible through our approach. In Fig. 6, the distributions for three different quantities are shown which were obtained upon pooled clustering runs across all subjects with kernel PCA preprocessing. Subplot (A) reports the distribution of within-cluster average decoding accuracies. The distribution starts with values above the applied threshold criterion (marked in red). Subplot (B) reveals the average within-cluster central frequency. Combining this with the insight that within-cluster variations with respect to the central frequency parameter  $f_0$  are rather small (see Fig. 8(C) later on), the distribution in (B) shows the probability of finding clusters in specific frequency ranges. The distribution is slightly dominated by alpha- and beta-band frequencies. Subplot (C) reveals the log-scaled distribution of the within-cluster regularization parameter utilized for the NTik-SPoC filter optimization. Its distribution is in good accordance with parameter ranges that were reported as suitable in our earlier work [39].

*3.1.4. Comparing the total number of clusters* For each of the 18 subjects, Fig. 7(A) reports the subject-specific number of configurations  $|\Omega_{sel}|$  which survived the two



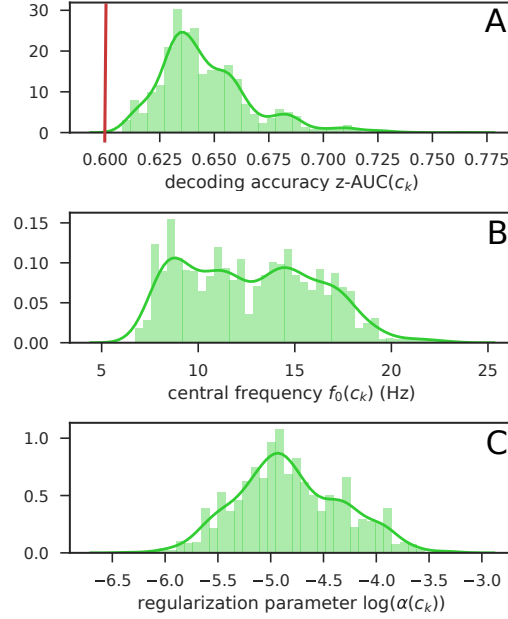


**Figure 6:** Cluster characterization by investigating the within-cluster mean value distribution of various parameters on pooled results for all clustering runs with kernel PCA. (A) reports the average within-cluster decoding accuracy (red line for z-AUC threshold), (B) shows the frequency range of mean central frequency values and (C) reports the log-scaled average regularization parameter utilized for NTik-SPoC optimization.

threshold criteria. The group average is reported by the black line with  $|\Omega_{sel,ga}| \approx 5,000$  configurations per subject which corresponds to approximately 6.2 % of the initial 81,000 explored configurations. We observed substantial differences across subjects regarding the total number of available robust oscillatory components. In Fig. 7(B), the average number of clusters resulting from multiple DBSCAN runs with 2000 randomly drawn configurations per subject are reported. As for subjects S2, S14 and S15 less than 2000 configurations were available, only a single DBSCAN run was performed. Across all subjects, applying PCA as preprocessing method elicits an average of  $|C|_{ga} = 3.9$  clusters, while kernel PCA almost doubles this number to 7.4 clusters. We want to emphasize, that we identified at least two clusters for each individual subject.

### 3.2. Group level validation of the method

For the validation of our proposed approach, we analyzed the final clustering results on a group level in two manners: First, the homogeneity of the clusters are investigated by multiple validation metrics. Second, the comparison of different validation metrics reveals information on the quality of clustering. The following group level evaluation is based on pooled results across all 18 subjects and the corresponding twelve repetitions.

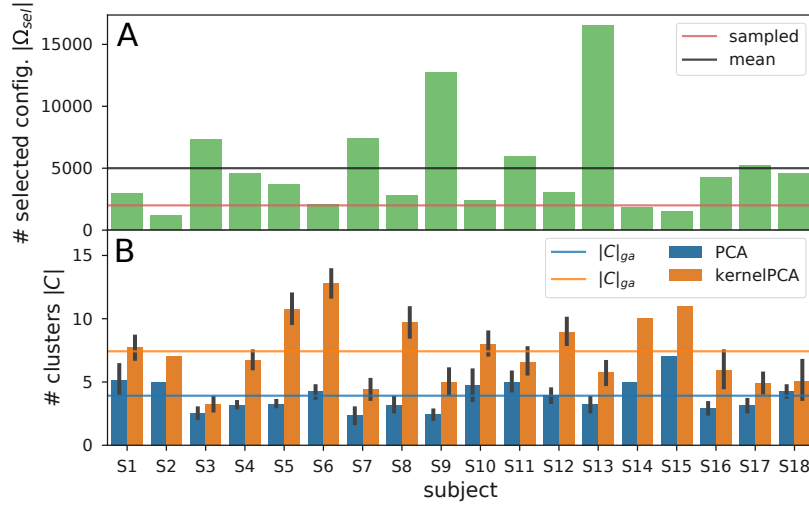


**Figure 7:** Group level analysis of the method: (A) Subject-wise total number of configurations/components after applying global threshold criteria. The black line indicates the average across all subjects, the red line marks the number of randomly sampled  $N = 2000$  components for a single clustering run. (B) Average number of clusters resulting from twelve DBSCAN evaluations for each subject and separately for two tested preprocessing methods (PCA / kernel PCA). For each bar, the black line reports the 95% confidence interval over twelve repetitions. The horizontal lines indicate the averages across subjects.

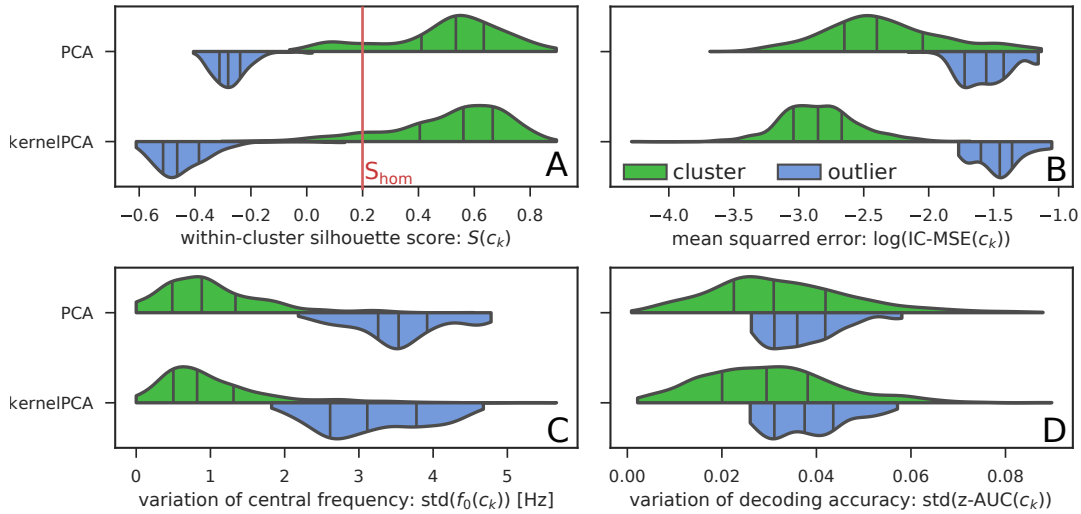


**Figure 8:** Contrasting distributions of multiple within-cluster evaluation metrics between clusters and outliers, pooled across subjects and twelve repetitions. Internal validation by average silhouette  $S(c_k)$  in (A). The vertical red line corresponds to the global silhouette threshold  $S_{hom}$ . As external validation, the log-scaled IC-MSE (B) is provided. In (C), the within-cluster central frequency variation  $\text{std}(f_0(c_k))$  and in (D) the variation  $\text{std}(z\text{-AUC}(c_k))$  are shown. Upon each validation metric, the results emerging from PCA preprocessing are contrasted to the ones of kernel PCA. For each violin plot, the vertical lines refer to the two quartiles and the median.

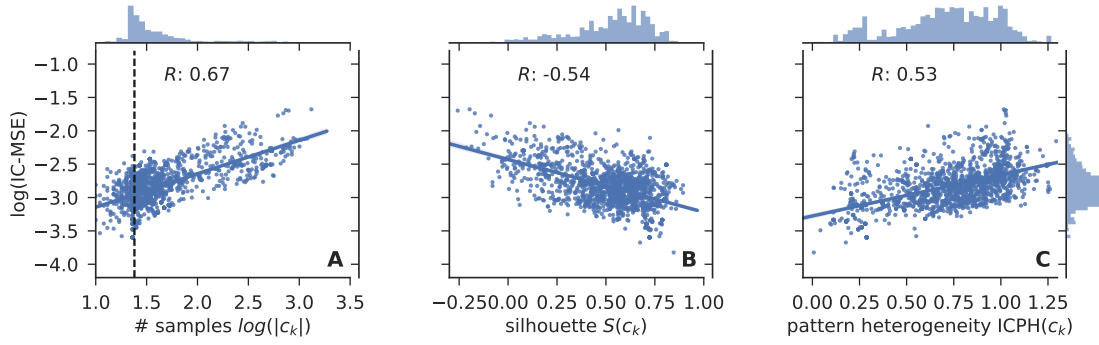


**Figure 9:** Group-level analysis of cluster (validation) metrics. Each data point refers to one single cluster resulting of all performed clustering runs across subjects with kernel PCA preprocessing. Outliers are not shown here. For all three subplots, the log-scaled IC-MSE is shown on the y-axis. Three different interactions are shown and the corresponding correlation is reported: (A) is referenced against the log-scaled cluster size  $|c_k|$ . The dashed line displays the DBSCAN parameter  $m_{pts} = 24$ . In (B), IC-MSE is referenced against the within-cluster silhouette  $S(c_k)$  and (C) shows the interplay with the pattern heterogeneity  $ICPH(c_k)$ . For each of the four metrics, the corresponding distributions are reported.

**3.2.1. Homogeneity of clusters** DBSCAN separates between cluster and outlier samples. In Fig. 8, the distributions for three types of metrics (see Sec. 2.3) are contrasted for all identified clusters against detected outlier sets. In addition, the metrics are compared between the two applied dimensionality reduction methods. (A) depicts the distribution for the within-cluster silhouette  $S(c_k)$ . As enforced by the applied selection criteria for  $\epsilon^*$ , the distribution of  $S(c_k)$  across all clusters is mostly above the subject-independent threshold criteria  $S_{hom} = 0.2$ , while the outlier distribution (blue) is mostly negative. In (B), the distribution of the within-cluster IC-MSE is shown. In accordance with the silhouette distribution in (A) but in reverse direction, the IC-MSE distribution is strictly shifted towards lower values compared to the outlier class. (C) reports the variation of the central frequency  $\text{std}(f_0(c_k))$  which is consistently below 3 Hz for clusters. (D) shows the distribution of decoding accuracy variations which on average are on a broader scale for the cluster class compared to the outlier clusters. When comparing the two preprocessing methods across the subplots (A)–(C), we observed that kernel PCA results in more favorable partitionings than PCA. This is documented by, e.g., larger silhouette values in (A) or smaller IC-MSE values in (B). Unless noted otherwise, we report results based on kernel PCA.

**3.2.2. Comparing cluster (validation) metrics** The interaction between the external validation metric IC-MSE to the cluster size  $|c_k|$  and two other evaluation metrics (see Sec. 2.3) is reported in Fig. 9. In (A), the averaged envelope homogeneity revealed by the IC-MSE is strongly dependent on the number of samples  $|c_k|$  of the respective cluster. The smaller the cluster size, the more probable it is to find a homogeneous cluster. The

dashed line in (A) reports the DBSCAN parameter  $m_{pts} = 24$ . If border points are within the  $\epsilon$ -neighborhood of core points of multiple clusters, they will be only assigned to one of them [43]. Thus, we find cluster sizes smaller than  $m_{pts}$ . Plot (B) shows a negative correlation of the external IC-MSE metric with the internal silhouette score which was used for DBSCAN optimization. The larger the silhouette value, the smaller the IC-MSE. Similarly observable from (C), there is a comparable positive correlation between the IC-MSE and the pattern heterogeneity. For small IC-MSE values, a high pattern homogeneity (reflected by low values) is found. However, there are also several cases with low IC-MSE but substantial pattern heterogeneity.

#### 4. Discussion

In summary, we propose a method for an informed component selection. Precisely, it identifies groups of oscillatory components that satisfy two optimization criteria: (a) they are required to have a robust decoding performance, and (b) they need to reflect functional relevance for the given experimental task.

Applying these two criteria, we demonstrate that the event-related envelope dynamics of oscillatory components provides a rich source of information, as these dynamics are strictly time-locked to within-trial events of a complex behavioral task. In addition, we show how this information can be exploited to identify functionally relevant and reliable oscillatory features from a large hyperparameter space. Thereby, our data-driven approach is capable to deal with the noisy character of EEG data and successfully reduces the probability to miss important, functionally relevant features.

On the level of individual subjects, the proposed approach allowed us to identify seven individual subsets of the configuration space on average. The approach ensured that these subsets elicit *robust* oscillatory features of homogeneous envelope dynamics. For this reason, it was necessary to design the approach such that it can explicitly cope with rank instabilities as these typically are observed when dealing with eigenvalue decompositions on real-world data sets [32]. These instabilities are commonly caused by slight variations of the training data set, or when non-deterministic decoding approaches are utilized.

##### 4.1. Within-trial structure could reveal individual behavioral strategies

Based on the studied SVIPT paradigm, the envelope plots in Fig. 4 show that the ERS effect towards the trial end can be time-locked to either *hit 3* or to *hit 4*, depending on the subject. This example nicely illustrates that our method is capable to extract the active phase of specific functional components with a high temporal precision. Interestingly, for comparisons across subjects, we might resolve different individual strategies. From a behavioral point of view, reaching event *hit 4* merely requires to completely release the force sensor. Users could fulfill *hit 4* with or without utilizing visual cursor feedback. Thus, it may be assumed that subject S7 (clusters C4, C5) did not rely on visual

feedback for the final hit event, leading to an ERS that started as early as the *hit 3* event.

#### 4.2. Features to assess the functional role of oscillatory brain signals

As discussed for the examples given in Fig. 4, exclusively utilizing the within-trial event-related envelope dynamics for clustering and not, e.g., scalp patterns turned out to be a suitable choice for our data scenario. In Fig. 9(B), we reported that single clusters can contain rather heterogeneous spatial activity patterns. This could mean that the neural origins of these oscillatory components differ despite the similarity in ERD/ERS features [14]. Accordingly, Bigdely-Shamlo et al. showed that it might be beneficial to additionally consider 3D dipole locations for clustering, which result from a source reconstruction step [28]. We agree on this view, as specifically from a clinical perspective knowledge about functional brain regions could provide added value. However, source reconstruction comes at a price, as results are sensitive to initial assumptions and raw signal quality, among others [52, 53]. As additional source features would have enlarged our dimensionality, here we decided against including them into our feature vectors. Moreover, the results by Onton et al. [14] also support the view that solely event-related dynamics might be sufficient to assess the functional role of oscillatory EEG features. Our observations support this judgment in the context of the investigated behavioral task.

Beside the utilized spectral envelope features, we did *not* include explicit frequency parameters into the feature representation for the clustering. Such explicit features, however, might be beneficial to add when dealing with clusterings across subjects or across multiple sessions of the same subject, as it may support to match corresponding components. Notably, our results show that the discovered clusters comprise components with highly similar, strictly confined frequency ranges. From a neurophysiological perspective, this finding is very plausible as rhythmic brain activity is well-known to be frequency-specific [1]. Overall, most clusters were found to represent oscillations of the alpha- and beta range. This finding is in accordance with an earlier analysis of the predictive oscillatory EEG features to explain trial-wise motor performance in SVIPT [32].

#### 4.3. Design choices for the clustering step

The clustering step required a limitation of the input dimensionality of the envelope features [42]. In this context, we contrasted the performance of PCA and kernel PCA for reducing the feature vectors down to 10 dimensions. We found that the use of kernel PCA almost doubled the amount of resulting clusters compared to PCA. Furthermore, clusters detected after condensation with kernel PCA were found to be more *homogeneous* than those resulting from PCA preprocessing (see Fig. 8). This finding might indicate that the ERD/ERS features contain non-linear structure which is valuable to retain for the clustering.

While the literature on clustering of brain signal features is mostly dominated by the k-means approach [27, 29], we chose the density-based DBSCAN algorithm for various reasons. First, DBSCAN does not assign each data sample to a cluster. Beside dense clusters, it handles outlier samples without assumptions about the global distribution of outliers. This is beneficial for our data scenario, as we can not expect every configuration to display well-defined envelope dynamics. Second, as DBSCAN does not make an explicit assumption about cluster shapes it copes well with non-linearly separable clusters. In contrast, k-means is biased towards convex cluster shapes and may not deal well with non-convex shapes. Third, DBSCAN does not require to specify the optimal number of clusters beforehand as a hyperparameter. Given our clustering scenario, this would be difficult to predict. Motivated by similar arguments, Bigdely-Shamlo et al. [28] utilized an affinity propagation clustering to circumvent the aforementioned shortcomings of k-means.

Revisiting our complete approach, we find several hyperparameters which influence the outcome of the final clustering step. Among others, these comprise the number and width of the time intervals for the temporal subsampling (see Fig. 3) as well as the number of components  $D_{red}$  obtained from the dimensionality reduction step. The choice of these hyperparameters reveals a trade-off between a sufficiently good temporal resolution of the envelope dynamics and avoiding the curse of dimensionality for large feature dimensions [54]. In principle, the framework could be further optimized by, e.g., maximizing the correlation between within-cluster silhouette scores and the IC-MSE scores.

#### 4.4. Method applicable for within- and across-subject clusterings

To allow for a group-level analysis as well as for comparisons between subjects and single subject analyses, we decided to create equally sized data sets before running DBSCAN. For all but three subjects this requirement lead to a downsampling of components, and we are aware, that we may have omitted informative data especially for subjects with a large component space (see Fig. 7). The repeated downsampling (an ordered random subset selection to  $\Omega_{sel}$ ) typically resulted in quite disjoint subsets, and each of them translated into different clusterings. But even if the 2000 samples drawn were almost identical between repetitions (as, e.g., for subject S6), small variations in the data set order can cause that border points are assigned to different classes [44]. Both cases contribute to the variation of the total number of clusters  $|C|$  that was observed within each subject. This variation, however, does not influence the applicability of our method.

While we restricted the analysis to within-subject clustering, the proposed approach can also be applied to perform across-subject clusterings in the future [29]. However, this scenario is more challenging due to strong subject-to-subject variations in brain activity caused by, e.g., anatomical differences which evoke different scalp projections [28, 21] of the same functional sources.

#### 4.5. Many complex tasks provide a rich inner structure

One key ingredient of this paper is the exploitation of the rich within-trial event structure of tasks such as SVIPT (see Fig. 1). This structure is defined by the sequence of events that occur along a single SVIPT trial. These multiple events offer a large number of choices when it comes to extracting ERD/ERS features: oscillatory activity could have been extracted not only for hit events, but in addition also aligned to error events (such as when the cursor overshoots a target field) or other application-specific events. The proposed analysis concept should generally be applicable to many complex real-world tasks, as long as they reveal sub steps that can be utilized to define a “within-task” event structure. For some real-world tasks the definition of “within-task” structure might not be as straightforward or temporal markers of subtasks may not have been recorded. In these cases we propose to consider implicit behavior such as eye movements to identify sub-steps of an underlying task. Exploiting this additional information, current brain state decoding approaches might gain access to the underlying functional role of features [55].

#### 4.6. Identifying functional roles of components on novel data

Assuming we apply our method on novel data, we propose a simple two-step procedure for identifying functionally relevant components: First, the *reliability* of the identified clusters needs to be verified, e.g., using the external IC-MSE metric. A comparison to the distribution reported in Fig. 9 will enable to judge its reliability. Second, one can assess the functional contribution of a cluster’s components by investigating the *ERD/ERS characteristics*. Functionally relevant components should reveal amplitude modulations time-locked to at least a few within-trial events (see Fig. 4 and Fig. 5). Along this line, the exact timing of ERD/ERS effects might provide valuable additional information.

#### 4.7. Expected benefit for targeted closed-loop interaction

Our method can provide a valuable offline tool to prepare informed closed-loop interaction protocols. To state an example, we foresee a potential benefit in the field of BCI protocols for stroke rehabilitation training [56, 57], where our method could be beneficial in multiple ways. First, it can allow to introspect the training progress by monitoring underlying cortical processes across multiple sessions. As an example, the introspective character of our method may allow contributing to the current debate on judging the role of ipsilesional versus contralesional features to trigger sensory feedback in rehabilitation scenarios after stroke [58]. Second, it may help to increase the efficacy of current BCI systems as it allows for an informed feature selection such that functionally specific BCI feedback can be targeted.

## 5. Conclusion

We presented a novel data-driven method for assessing reliable and functionally relevant oscillatory EEG components based on a spatial filtering approach. For this purpose, we first embrace the large variability of spatial filters before condensing the information by a density-based clustering on components' functional signatures. For the condensing, we make use of within-trial structure, which we have exemplified for a hand force task in which inner structure translates into rich temporal dynamics of oscillatory components. Our analysis finally reveals homogeneous sets of components which evoke robust oscillatory features with distinct envelope dynamics.

This approach should be applicable to any choice of spatial filtering algorithm under investigation. As our method provides individual introspection about the functional role of components, we see a potential practical benefit by increasing the efficacy of closed-loop protocols, and thereby finally ensuring a targeted and subject-specific user feedback. This may be of specific importance for novel protocols in stroke rehabilitation.

## Acknowledgements

This work was supported by BrainLinks-BrainTools Cluster of Excellence funded by the German Research Foundation (DFG, grant number EXC 1086) and the project SuitAble (DFG, grant number 387670982). The authors also acknowledge support by the state of Baden-Württemberg, Germany, through bwHPC and the German Research Foundation (DFG, INST 39/963-1 FUGG) The oscillatory component extraction was partly performed with the MATLAB-based BBCI toolbox [59], while the clustering analysis was realized within the scikit-learn framework [60].

## References

- [1] György Buzsáki. *Rhythms of the Brain*. Oxford University Press, 2006.
- [2] Xiao-Jing Wang. Neurophysiological and Computational Principles of Cortical Rhythms in Cognition. *Physiological Reviews*, 90(3):1195–1268, July 2010.
- [3] Fernando Lopes da Silva. EEG and MEG: Relevance to Neuroscience. *Neuron*, 80(5):1112–1128, December 2013.
- [4] Hanneke van Dijk, Jan-Mathijs Schoffelen, Robert Oostenveld, and Ole Jensen. Prestimulus oscillatory activity in the alpha band predicts visual discrimination ability. *The Journal of Neuroscience*, 28(8):1816–1823, 2008.
- [5] Christoph S. Herrmann, Daniel Strüber, Randolph F. Helfrich, and Andreas K. Engel. EEG oscillations: From correlation to causality. *International Journal of Psychophysiology*, 103:12–21, May 2016.
- [6] G. Pfurtscheller. Graphical display and statistical evaluation of event-related desynchronization (ERD). *Electroencephalography and Clinical Neurophysiology*, 43(5):757–760, November 1977.
- [7] Gert Pfurtscheller and FH Lopes Da Silva. Event-related EEG/MEG synchronization and desynchronization: basic principles. *Clinical Neurophysiology*, 110(11):1842–1857, 1999.
- [8] C Neuper and G Pfurtscheller. Event-related dynamics of cortical rhythms: frequency-specific features and functional correlates. *International Journal of Psychophysiology*, 43(1):41–58, December 2001.



- [9] B. Graitmann and G. Pfurtscheller. Quantification and visualization of event-related changes in oscillatory brain activity in the time-frequency domain. *Progress in brain research*, 159:79, 2006.
- [10] Steven Lemm, Klaus-Robert Müller, and Gabriel Curio. A Generalized Framework for Quantifying the Dynamics of EEG Event-Related Desynchronization. *PLoS Computational Biology*, 5(8), August 2009.
- [11] Scott Makeig. Auditory event-related dynamics of the EEG spectrum and effects of exposure to tones. *Electroencephalography and Clinical Neurophysiology*, 86(4):283–293, April 1993.
- [12] Scott Makeig, Stefan Debener, Julie Onton, and Arnaud Delorme. Mining event-related brain dynamics. *Trends in Cognitive Sciences*, 8(5):204–210, May 2004.
- [13] Martin Seeber, Reinhold Scherer, and Gernot R. Müller-Putz. EEG Oscillations Are Modulated in Different Behavior-Related Networks during Rhythmic Finger Movements. *Journal of Neuroscience*, 36(46):11671–11681, November 2016.
- [14] Julie Onton and Scott Makeig. Information-based modeling of event-related brain dynamics. In Christa Neuper and Wolfgang Klimesch, editors, *Progress in Brain Research*, volume 159 of *Event-Related Dynamics of Brain Oscillations*, pages 99–120. Elsevier, January 2006.
- [15] Benjamin Blankertz, Ryota Tomioka, Steven Lemm, Motoaki Kawanabe, and Klaus-Robert Müller. Optimizing spatial filters for robust EEG single-trial analysis. *Signal Processing Magazine, IEEE*, 25(1):41–56, 2008.
- [16] Alain de Cheveigné and Lucas C. Parra. Joint decorrelation, a versatile tool for multichannel data analysis. *NeuroImage*, 98(Supplement C):487–505, September 2014.
- [17] Peter W. Donhauser, Esther Florin, and Sylvain Baillet. Imaging of neural oscillations with embedded inferential and group prevalence statistics. *PLOS Computational Biology*, 14(2):e1005990, February 2018.
- [18] Stefan Haufe, Frank Meinecke, Kai Görden, Sven Dähne, John-Dylan Haynes, Benjamin Blankertz, and Felix Bießmann. On the interpretation of weight vectors of linear models in multivariate neuroimaging. *NeuroImage*, 87(0):96 – 110, 2014.
- [19] Surjo R. Soekadar, Niels Birbaumer, Marc W. Slutzky, and Leonardo G. Cohen. Brain-machine interfaces in neurorehabilitation of stroke. *Neurobiology of Disease*, 83:172–179, November 2015.
- [20] Alain de Cheveigné and Dorothee Arzounian. Scanning for oscillations. *Journal of Neural Engineering*, 12(6):066020, 2015.
- [21] Fiorenzo Artoni, Danilo Menicucci, Arnaud Delorme, Scott Makeig, and Silvestro Micera. RELICA: A method for estimating the reliability of independent components. *NeuroImage*, 103:391–400, December 2014.
- [22] Juan Sebastián Castaño-Candamil, Andreas Meinel, Sven Dähne, and Michael Tangermann. Probing meaningfulness of oscillatory EEG components with bootstrapping, label noise and reduced training sets. In *Engineering in Medicine and Biology Society (EMBC), 2015 37th Annual International Conference of the IEEE*, pages 5159–5162. IEEE, 2015.
- [23] Stefan Debener, Markus Ullsperger, Markus Siegel, and Andreas K. Engel. Single-trial EEGfMRI reveals the dynamics of cognitive function. *Trends in Cognitive Sciences*, 10(12):558–563, December 2006.
- [24] Matthias Krauledat, Michael Tangermann, Benjamin Blankertz, and Klaus-Robert Müller. Towards zero training for brain-computer interfacing. *PLoS ONE*, 3(8):e2967, 08 2008.
- [25] Stefan Harmeling, Guido Dornhege, David Tax, Frank Meinecke, and Klaus-Robert Müller. From outliers to prototypes: Ordering data. *Neurocomputing*, 69(13):1608–1618, August 2006.
- [26] Tomasz M. Rutkowski, Danilo P. Mandic, Andrzej Cichocki, and Andrzej W. Przybyszewski. Emd approach to multichannel eeg data the amplitude and phase components clustering analysis. *Journal of Circuits, Systems and Computers*, 19(01):215–229, February 2010.
- [27] Sara Spadone, Francesco de Pasquale, Dante Mantini, and Stefania Della Penna. A K-means multivariate approach for clustering independent components from magnetoencephalographic data. *NeuroImage*, 62(3):1912–1923, September 2012.
- [28] Nima Bigdely-Shamlo, Tim Mullen, Kenneth Kreutz-Delgado, and Scott Makeig. Measure

- projection analysis: A probabilistic approach to EEG source comparison and multi-subject inference. *NeuroImage*, 72:287–303, May 2013.
- [29] Jon Touryan, Brent J. Lance, Scott E. Kerick, Anthony J. Ries, and Kaleb McDowell. Common EEG features for behavioral estimation in disparate, real-world tasks. *Biological Psychology*, 114:93–107, February 2016.
  - [30] Feng Rong and José L. Contreras-Vidal. Magnetoencephalographic artifact identification and automatic removal based on independent component analysis and categorization approaches. *Journal of Neuroscience Methods*, 157(2):337–354, October 2006.
  - [31] Janine Reis, Heidi M. Schambra, Leonardo G. Cohen, Ethan R. Buch, Brita Fritsch, Eric Zarahn, Pablo A. Celnik, and John W. Krakauer. Noninvasive cortical stimulation enhances motor skill acquisition over multiple days through an effect on consolidation. *Proceedings of the National Academy of Sciences*, 106(5):1590–1595, 2009.
  - [32] Andreas Meinel, Sebastián Castaño-Candamil, Janine Reis, and Michael Tangermann. Pre-trial EEG-based single-trial motor performance prediction to enhance neuroergonomics for a hand force task. *Frontiers in Human Neuroscience*, 10:170, 2016.
  - [33] I. Winkler, S. Debener, K. R. Müller, and M. Tangermann. On the influence of high-pass filtering on ICA-based artifact reduction in EEG-ERP. In *2015 37th Annual International Conference of the IEEE Engineering in Medicine and Biology Society (EMBC)*, pages 4101–4105, August 2015.
  - [34] Irene Winkler, Stephanie Brandl, Franziska Horn, Eric Waldburger, Carsten Allefeld, and Michael Tangermann. Robust artifactual independent component classification for BCI practitioners. *Journal of Neural Engineering*, 11(3):035013, 2014.
  - [35] Lucas C Parra, Clay D Spence, Adam D Gerson, and Paul Sajda. Recipes for the linear analysis of EEG. *NeuroImage*, 28(2):326–341, 2005.
  - [36] N. M. Correa, T. Adali, Y. O. Li, and V. D. Calhoun. Canonical Correlation Analysis for Data Fusion and Group Inferences. *IEEE Signal Processing Magazine*, 27(4):39–50, 2010.
  - [37] F. Lotte and C. Guan. Regularizing common spatial patterns to improve BCI designs: Unified theory and new algorithms. *IEEE Transactions on Biomedical Engineering*, 58(2):355–362, Feb 2011.
  - [38] Sven Dähne, Frank C. Meinecke, Stefan Haufe, Johannes Höhne, Michael Tangermann, Klaus-Robert Müller, and Vadim V. Nikulin. SPoC: a novel framework for relating the amplitude of neuronal oscillations to behaviorally relevant parameters. *NeuroImage*, 86(0):111–122, 2014.
  - [39] Andreas Meinel, Sebastián Castaño-Candamil, Benjamin Blankertz, Fabien Lotte, and Michael Tangermann. Characterizing regularization techniques for spatial filter optimization in oscillatory EEG regression problems. (*manuscript submitted for publication*), 2018.
  - [40] A. Meinel, F. Lotte, and M. Tangermann. Tikhonov regularization enhances EEG-based spatial filtering for single-trial regression. In *Proceedings of the 7th Graz Brain-Computer interface Conference 2017*, pages 308–313, 2017.
  - [41] Tom Fawcett. An introduction to ROC analysis. *Pattern Recognition Letters*, 27(8):861–874, 2006.
  - [42] T. Warren Liao. Clustering of time series dataa survey. *Pattern Recognition*, 38(11):1857–1874, November 2005.
  - [43] Martin Ester, Hans-Peter Kriegel, Jörg Sander, and Xiaowei Xu. A density-based algorithm for discovering clusters in large spatial databases with noise. In *Kdd*, volume 96, pages 226–231, 1996.
  - [44] Erich Schubert, Jörg Sander, Martin Ester, Hans Peter Kriegel, and Xiaowei Xu. DBSCAN Revisited, Revisited: Why and How You Should (Still) Use DBSCAN. *ACM Trans. Database Syst.*, 42(3):19:1–19:21, July 2017.
  - [45] Hans-Peter Kriegel, Peer Kröger, Jörg Sander, and Arthur Zimek. Density-based clustering. *Wiley Interdisciplinary Reviews: Data Mining and Knowledge Discovery*, 1(3):231–240, 2011.
  - [46] Jörg Sander, Martin Ester, Hans-Peter Kriegel, and Xiaowei Xu. Density-Based Clustering

- in Spatial Databases: The Algorithm GDBSCAN and Its Applications. *Data Mining and Knowledge Discovery*, 2(2):169–194, June 1998.
- [47] M. Halkidi and M. Vazirgiannis. Clustering validity assessment: finding the optimal partitioning of a data set. In *Proceedings 2001 IEEE International Conference on Data Mining*, pages 187–194, 2001.
  - [48] D. Moulavi, P. Jaskowiak, R. Campello, A. Zimek, and J. Sander. Density-Based Clustering Validation. In *Proceedings of the 2014 SIAM International Conference on Data Mining*, Proceedings, pages 839–847. Society for Industrial and Applied Mathematics, April 2014.
  - [49] Olatz Arbelaiz, Ibai Gurrutxaga, Javier Muguerza, Jesús M. Pérez, and Iñigo Perona. An extensive comparative study of cluster validity indices. *Pattern Recognition*, 46(1):243–256, 2013.
  - [50] Peter J. Rousseeuw. Silhouettes: a graphical aid to the interpretation and validation of cluster analysis. *Journal of computational and applied mathematics*, 20:53–65, 1987.
  - [51] Y. Liu, Z. Li, H. Xiong, X. Gao, and J. Wu. Understanding of Internal Clustering Validation Measures. In *2010 IEEE International Conference on Data Mining*, pages 911–916, December 2010.
  - [52] Sebastián Castao-Candamil, Johannes Höhne, Juan-David Martínez-Vargas, Xing-Wei An, German Castellanos-Domínguez, and Stefan Haufe. Solving the EEG inverse problem based on spacetimefrequency structured sparsity constraints. *NeuroImage*, 118:598–612, September 2015.
  - [53] Keyvan Mahjoory, Vadim V. Nikulin, Loc Botrel, Klaus Linkenkaer-Hansen, Marco M. Fato, and Stefan Haufe. Consistency of EEG source localization and connectivity estimates. *NeuroImage*, 152:590–601, May 2017.
  - [54] Charu C. Aggarwal, Alexander Hinneburg, and Daniel A. Keim. On the Surprising Behavior of Distance Metrics in High Dimensional Space. In *Database Theory ICDT 2001*, Lecture Notes in Computer Science, pages 420–434. Springer, Berlin, Heidelberg, January 2001.
  - [55] S. Makeig, C. Kothe, T. Mullen, N. Bigdely-Shamlo, Z. Zhang, and K. Kreutz-Delgado. Evolving signal processing for brain-computer interfaces. *Proceedings of the IEEE*, 100(Special Centennial Issue):1567–1584, May 2012.
  - [56] Clemens Brunner, Niels Birbaumer, Benjamin Blankertz, Christoph Guger, Andrea Kübler, Donatella Mattia, José del R. Millán, Felip Miralles, Anton Nijholt, Eloy Opisso, Nick Ramsey, Patric Salomon, and Gernot R. Müller-Putz. BNCI Horizon 2020: towards a roadmap for the BCI community. *Brain-Computer Interfaces*, 2(1):1–10, January 2015.
  - [57] Alexander Remsik, Brittany Young, Rebecca Vermilyea, Laura Kiekhoefer, Jessica Abrams, Samantha Evander Elmore, Paige Schultz, Veena Nair, Dorothy Edwards, Justin Williams, and Vivek Prabhakaran. A review of the progression and future implications of brain-computer interface therapies for restoration of distal upper extremity motor function after stroke. *Expert Review of Medical Devices*, 13(5):445–454, May 2016.
  - [58] Keith C. Dodd, Veena A. Nair, and Vivek Prabhakaran. Role of the Contralateral vs. Ipsilateral Hemisphere in Stroke Recovery. *Frontiers in Human Neuroscience*, 11, 2017.
  - [59] Benjamin Blankertz, Laura Acqualagna, Sven Dähne, Stefan Haufe, Matthias Schultze-Kraft, Irene Sturm, Marija Uumljic, Markus A. Wenzel, Gabriel Curio, and Klaus-Robert Müller. The berlin brain-computer interface: Progress beyond communication and control. *Frontiers in Neuroscience*, 10:530, 2016.
  - [60] F. Pedregosa, G. Varoquaux, A. Gramfort, V. Michel, B. Thirion, O. Grisel, M. Blondel, P. Prettenhofer, R. Weiss, V. Dubourg, J. Vanderplas, A. Passos, D. Cournapeau, M. Brucher, M. Perrot, and E. Duchesnay. Scikit-learn: Machine learning in Python. *Journal of Machine Learning Research*, 12:2825–2830, 2011.